Quantifying recombination and charge carrier extraction in halide perovskites via hyperspectral time-resolved photoluminescence imaging

Cite as: APL Energy 2, 016111 (2024); doi: 10.1063/5.0188166
Submitted: 20 November 2023 • Accepted: 29 February 2024 •
Published Online: 21 March 2024

H. Phirke,[1,a] S. Gharabeiki,[1] A. Singh,[1] A. Krishna,[2] S. Siebentritt,[1] and A. Redinger[1,b]

AFFILIATIONS

[1] Department of Physics and Materials Science, University of Luxembourg, Luxembourg City L-1511, Luxembourg
[2] Institute of Chemical Sciences and Engineering, École Polytechnique Fédérale de Lausanne, Lausanne 1015, Switzerland

[a] Author to whom correspondence should be addressed: himanshu.phirke@uni.lu
[b] Electronic mail: alex.redinger@uni.lu

ABSTRACT

Identifying sources of nonradiative recombination and quantifying charge carrier extraction in halide perovskite solar cells are important in further developing this thin-film technology. Steady-state and time-resolved photoluminescence (TRPL), in combination with analytical modeling, have emerged as non-destructive tools to achieve the desired results. However, the exact location of the recombination and charge carrier extraction losses in devices is often obscured by various competing processes when photoluminescence measurements are analyzed. Here, we show via absolute-photon-calibrated hyperspectral photoluminescence and TRPL imaging how surface passivation and inhomogeneities at interfaces impact the photoluminescence quantum yields and minority carrier lifetimes. Laser illumination from the perovskite and glass/TiO_2 sides allows us to disentangle changes in surface recombination velocity from the charge carrier extraction at the electron transport layer. We find that charge extraction is spatially modulated due to an inhomogeneous mesoporous (mp)-TiO_2 film thickness. Our results show that the mp-TiO_2 layer is not fully optimized since the electronic properties are spatially modified, leading to lateral changes in quasi-Fermi-level splitting, minority carrier lifetime and, consequently, a reduction in open-circuit voltage.

I. INTRODUCTION

Hybrid perovskite solar cells have attracted tremendous attention in the scientific community over the past decade due to an unprecedented increase in power conversion efficiency, reaching 26% in the laboratory and 18.6% on modules.[1] The relatively simple and inexpensive fabrication of devices through solution processing,[2] together with the tunability of the bandgap by chemical substitution,[3–5] has made perovskites very attractive materials in many applications such as photovoltaics, light-emitting diodes,[6] lasers,[7] and photodetectors.[8] They have remarkable characteristics such as long diffusion lengths,[9] low exciton binding energies,[10] and long carrier lifetimes exceeding 1 μs.[11,12]

As perovskite solar cells become more and more efficient, surpassing the 25% efficiency benchmark, each layer and its properties need to be optimized to the highest level in order to further reduce the gap to the theoretical power conversion efficiency limit. The bulk, interfaces, and extraction layers need to be optimized to reduce nonradiative recombination, and the selective extraction of holes and electrons needs to be maximized, while the interface defect densities need to be kept to a minimum. In addition, all of the material properties need to be homogeneous on the length scale of full devices and, eventually, even full-size modules to achieve maximum performance. Consequently, high-resolution mapping techniques will become increasingly important.

The key techniques to assess recombination losses in solar cell devices are steady-state and time-resolved photoluminescence (PL and TRPL).[13] They allow for contactless measurements of charge carrier recombination processes of films on glass, layer stacks, and complete devices, making them ideal tools for material

characterization and optimization. Although TRPL is a commonly utilized method for determining the recombination coefficients and charge carrier lifetimes in halide perovskites and other semiconductors, the interpretation of the measured transients is not straightforward, and the characteristic decay time is often not equal to the minority carrier lifetime of the perovskite absorber. The injection level,[14,15] the surface recombination velocity, interface recombination,[16] charge carrier separation and extraction, and interface charging[17–19] must be taken into account to correctly interpret the measurements. In recent years, powerful numerical simulations have been developed that give clear guidelines for analyzing and interpreting TRPL transients measured on perovskite absorbers, including extraction layers.[18] Combining the knowledge gained from simulations with measurements performed under specific illumination conditions allows us to pinpoint the current bottleneck of the absorber layers with high accuracy.

Furthermore, quantifying lateral inhomogeneities in solar cells is increasingly important. To gain access to laterally resolved PL and TRPL results, hyperspectral photoluminescence imaging, or lifetime mapping, has been developed[20,21] that allows us to study all the quantities mentioned earlier as a function of position, ranging from sub-micrometer properties[22,23] to full devices,[24] wafers,[25] and even full-size modules.[26] Results on grain boundary activity,[22] lateral heterogeneities,[27,28] variations in series resistance,[29] and reduction of nonradiative losses due to interface passivation[24,30] have been reported. On devices, voltage-dependent mapping techniques have also been used to identify differences in charge carrier extraction/selectivity.[31]

In this paper, we used time-resolved photoluminescence imaging to better understand the lateral inhomogeneities in state-of-the-art perovskite absorbers deposited on a TiO_2-based electron extraction layer. Samples with and without surface passivation layers were used to distinguish between surface recombination and charge carrier extraction. Previous studies have shown that perovskites deposited on TiO_2 exhibited lateral variations in PL.[31,32] To discriminate between surface recombination and carrier extraction, we collect the PL and TRPL signals by illuminating the sample from the front (perovskite) and backside (glass/TiO_2). We employ the established models to differentiate between surface recombination and carrier extraction. Our analysis shows that the TiO_2/perovskite interface is of high quality; however, the lateral variations lead to varying extraction efficiencies, which need to be circumvented to achieve even higher efficiencies.

II. EXPERIMENTAL

Photoluminescence imaging and transient photoluminescence measurements were performed using a custom-built hyperspectral imaging setup. The system consists of an intensified charged coupled device (iCCD) camera, a tunable liquid crystal filter operating in a spectral range of 650–1100 nm, a tube lens, and an objective lens. We used a pulsed 532 nm laser (VISUV-532-HP; pulse width<1ns) to illuminate the sample with a beam size of 7×7 mm^2. The laser beam is further homogenized to have a uniform top-hat beam profile. The setup is calibrated for absolute photon counts, allowing the conversion of the raw intensity directly to a photoluminescence quantum yield Q_e^{lum}. A schematic of the photoluminescence setup is depicted in the supplementary material (Fig. S1).

The calibration to absolute photon numbers, Y_{PL}, was performed as follows. A small Ulbricht sphere with a diameter of 100 mm was placed below the camera system. A single opening facing the camera was put in focus with the camera, and in a first step, a white light source with a known spectrum was coupled into the sphere. This allowed us to correct for the measurements spectrally. In the second step, the spectrally corrected measurements needed to be calibrated to absolute photon numbers. Therefore, a 780 nm laser diode was coupled into the sphere, and a spectrally resolved measurement was carried out with the imaging system. The laser power exiting the sphere was measured with a power meter, allowing one to directly convert the measured counts to photon numbers. Finally, the impinging laser power hitting the sample was measured with a power meter at the position of the sample. This procedure allowed us to calculate the PL quantum yield as follows:

$$Q_e^{lum} = \frac{\int_0^\infty Y_{PL}(E)dE}{\int_0^\infty \phi_S(E)a(E)dE} \equiv \frac{\text{Number of emitted photons}}{\text{Number of absorbed photons}}. \quad (1)$$

The externally emitted photoluminescence yield is denoted as $Y_{PL}(E)$ whereas the sun's photon spectrum is $\Phi_s(E)$ and $a(E)$ is the absorptivity of the perovskite film. Measurements were carried out in two different modes. Imaging was carried out primarily by integrating the measured counts over a period of 1 s. The repetition frequency was set to 40 MHz to have a high photon flux and to be close to one sun equivalent condition, i.e., $1.7 \cdot 10^{21}$ (photons/m^2)/s for a bandgap of 1.57 eV. These measurements are used to deduce Q_e^{lum} values for the different types of absorbers. TRPL measurements were performed at a low repetition frequency of 750 kHz without a monochromator on the detection side. Here, the iCCD camera was used to trigger the laser, and photons were collected every 2.5 ns, with a gate width of 30 ns. This allowed us to collect laterally resolved transients with a time resolution of 2 ns, as deduced from the rising edge of the PL at the time the photon pulse hit the sample. The two methods allowed us to measure, on one hand, the laterally resolved Q_e^{lum} values, whereas the latter could be used to measure the transient behavior of the charge carriers. In order to compare the Q_e^{lum} values measured with the pulsed laser with those with a continuous-wave (CW) laser, the same sample was measured with a 637 nm CW laser operated at 0.5 and 1 sun equivalent conditions.

In this study, we used a $(FAPbI_3)_{0.97}(MAPbBr_3)_{0.03}$ perovskite deposited on a TiO_2 double layer consisting of a compact layer (c-TiO_2; 20–40 nm) and a mesoporous layer (mp-TiO_2; 100–150 nm). Details of the fabrication process and the device efficiencies (champion cell: 21.5%) can be found in Ref. 33. Surface passivation was accomplished by depositing a thin layer of biphenyl-4 4′-dithiol on top of the perovskite film, allowing higher efficiencies (champion cell: 23.8%), as reported in Ref. 34. All samples were stored in an N_2-filled glovebox and measured in N_2 or air, depending on the setup or geometry. We cross-checked that the samples did not degrade during the measurements in the air. Since mp-TiO_2 will be of special interest here, we briefly summarize the fabrication of this layer. The film was prepared with a commercial TiO_2 paste (Dyesol 30 NR-D) diluted in ethanol (1:6 weight ratio) and then spin-coated onto the c-TiO_2 layer. The films were then dried at 80 °C for 10 min, followed by sintering up to 450 °C. Finally, a 0.1M solution of Li-TFSI was spin-coated, followed by another sintering at 450 °C.

III. CONTINUOUS VS PULSED ILLUMINATION

Before presenting the actual imaging results, we need to discuss how the Q_e^{lum} values, measured with a pulsed laser (operated at 40 MHz) compared to measurements carried out with a continuous wave (CW-laser). In the community, the choice of a laser source to perform photoluminescence (PL) experiments has been a topic of considerable interest and debate.[19]

In Fig. 1(a), the integrated PL yield is plotted as a function of the laser flux on a double logarithmic scale, whereas quasi-Fermi-level splitting (μ_{QFL}) as a function of sun-equivalents is presented in Fig. 1(b). PL measurements with a pulsed laser at 532 nm and a CW-laser at 637 nm were performed in two independent absolute-photon calibrated PL setups. From a linear fit to the data in Fig. 1(a), an optical diode factor $k = 1.5$ is deduced. The two data points at $1.7 \cdot 10^{21}$ m^{-2} s^{-1} (1 sun equiv.) for both measurements are very close to each other and within the error bar of the calibration.

The measured PL yields can be converted to Q_e^{lum} via Eq. (1) and then into a quasi-Fermi-level via

$$\mu_{\mathrm{QFL}} = \mu_{\mathrm{QFL}}^{\mathrm{rad}} + kT \cdot \ln\left\{Q_e^{\mathrm{lum}}\right\}, \tag{2}$$

with $\mu_{\mathrm{QFL}}^{\mathrm{rad}}$ being the radiative limit at the respective injection. For the present work, the exact value of μ_{QFL} is not crucial, and in the following, we will restrict the discussion to values of Q_e^{lum}, which are independent of the exact absorber bandgap. The comparison shows that, for the present samples, the measurements carried out with a pulsed laser at a high repetition frequency can be considered quasi-static. This makes sense since the carrier lifetimes are very long (hundreds of nanoseconds, as will be shown in the following sections), which is much longer than the time difference between two consecutive pulses (25 ns).

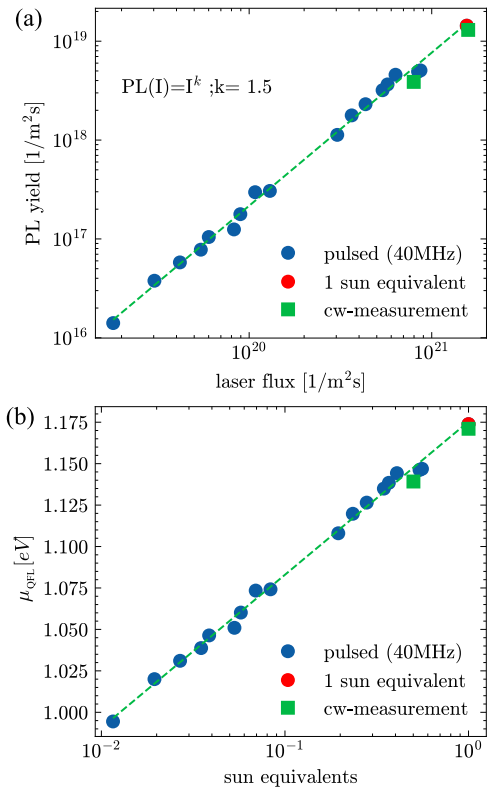

FIG. 1. (a) Integrated PL yield as a function of laser flux using a pulsed laser source at 40 MHz repetitive frequency at a wavelength of 532 nm compared to a CW-measurement carried out with a 637 nm laser. (b) Quasi Fermi-level splitting μ_{QFL} as a function of sun equivalent photon densities for CW and pulsed illumination.

IV. LATERALLY RESOLVED Q_e^{lum}-MAPS

Having established the relationship between pulsed and CW-laser illumination, we proceed with the laterally resolved measurements on the perovskite films. Figure 2 depicts the Q_e^{lum} maps measured under 68% of one sun equivalent illumination conditions of two perovskite absorbers. Our laser could not go further to complete one sun in injection during the period of these measurements. Figure 2(a) depicts the sample without a passivation layer, whereas Fig. 2(b) shows the result after surface passivation with the organic molecule. The respective PL spectrum of these samples can be found in the supplementary material (Fig. S2). In both images, we see a stripe pattern consistent with previous reports in which perovskite absorbers were spin-coated on a TiO_2 double layer.[31,34] In addition to the stripes, we find local inhomogeneities with either reduced or enhanced quantum yields. Spectrally resolved PL maps show very similar PL peak positions for the two absorbers at a photon energy of 1.56 eV, in good agreement with previous results.[33]

The most important difference between the two absorbers is the value of Q_e^{lum}, which is approximately an order of magnitude higher for the passivated absorber [Fig. 2(b)] compared to the non-passivated one [Fig. 2(a)]. In Figs. 2(c) and 2(d), the variations in Q_e^{lum} are represented as histograms. The average values $\overline{Q_e^{lum}}$ ($4.2 \cdot 10^{-4}$ vs $3.7 \cdot 10^{-3}$) coincide with the average color in Figs. 2(a) and 2(b), and we find a FWHM value, which is in both cases ~20% of the average value.

From these measurements, we can infer that the origin of the stripe-like pattern is not related to the perovskite surface since the addition of a passivation layer does not change the lateral variations in Q_e^{lum}. However, the number of possible reasons is still high. The deposition of the perovskite absorber could be inhomogeneous. This could be triggered by the spin coating of the perovskite or by the underlying TiO_2. On the other hand, TiO_2 could be inhomogeneous in thickness or the properties of TiO_2 change laterally, thus changing the recombination activity or charge extraction at the Electron transport layer (ETL) layer. To discriminate between the different possibilities, we need to discuss how the thickness and the surface recombination velocity are related to Q_e^{lum}. In general, Q_e^{lum} can be calculated via the following equation:[13]

$$Q_e^{lum} = \frac{p_e \cdot k_{rad} \cdot np}{\frac{\Delta n}{\tau_{\mathrm{eff}}} + (p_e + p_a) \cdot k_{rad} \cdot np}. \tag{3}$$

Assuming a p-type semiconductor, the hole density is denoted by $p = \Delta p + N_A$. In the case of high injection, the background doping is not relevant, and $n = p$ can be assumed. $\Delta n = (n - n_0)$ denotes the number of minority carriers in the system, which is given by the difference between the injected carriers and the equilibrium concentration of electrons in the semiconductor. The coefficient p_e defines

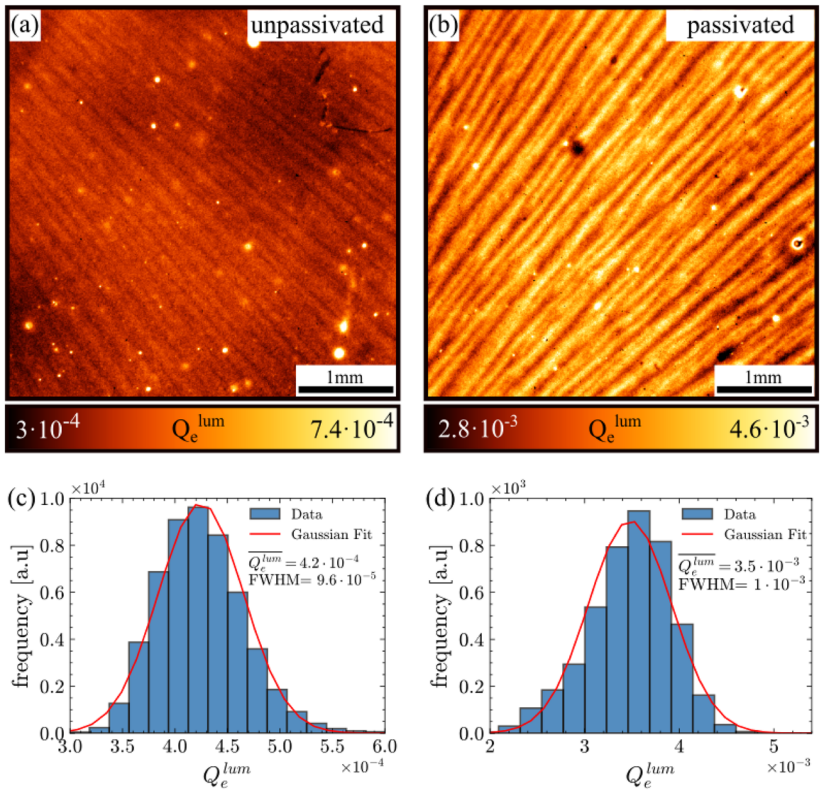

FIG. 2. Q_e^{lum} maps of (a) the unpassivated surface, (b) the passivated surface of the perovskite obtained by photoluminescence imaging, (c) and (d) are respective histograms of the Q_e^{lum} values including a Gaussian fit.

the probability of emission out of the semiconductor stack, while p_a is equal to the probability of re-absorption in additional layers of the stack, excluding the perovskite layer. The effective lifetime τ_{eff}, as defined by

$$\frac{1}{\tau_{eff}} = \frac{1}{\tau_{rad}} + \frac{1}{\tau_{nr}} + \frac{1}{\tau_{surf}}, \tag{4}$$

where τ_{rad} equals the radiative lifetime, τ_{nr} is the nonradiative lifetime of the bulk, and finally τ_{surf} is the surface-related part. Therefore, the lowest lifetime will dominate τ_{eff}. It is important to note that the surface-related term is thickness dependent [see Eq. (5)] and, therefore, any change in the thickness of the perovskite will change τ_{eff} in the case of dominant interface recombination. The two terms on the right side of Eq. (5) are related to the recombination process at the interface, limited by the magnitude of the surface recombination velocity S_n, and the transport to the surface, which scales quadratically with thickness d and inversely with the diffusion constant D_n,

$$\tau_{surf} = \frac{d}{2S_n} + \frac{d^2}{D_n \cdot \pi^2}. \tag{5}$$

From Eq. (5), we see that variations in the perovskite thickness may very well impact τ_{eff} and consequently also Q_e^{lum}. To check whether the thickness of the perovskite layer or the thickness of TiO_2 is non-homogeneous, the following experiment was carried out. A sample with TiO_2 and perovskite was first mechanically scratched with a sharp knife, and a profilometer measurement perpendicular to the scratch was performed. The scratch was clearly visible in the optical image of the profilometer setup [Fig. 3(b)]. The measured profile is plotted in Fig. 3(a) in blue.

In a subsequent step, the perovskite layer was removed by dipping the sample in Dimethyl-formamide (DMF), allowing us to measure the corrugation of the mesoporous-TiO_2 in the same spot [Fig. 3(a), green line]. An image of the mesoporous-TiO_2 surface after the DMF treatment can be found in the supplementary material (Fig. S3). The comparison between the two curves showed that the height changes observed on the perovskite surface are due to the corrugation of the mp-TiO_2. From this set of measurements, we were also able to deduce the perovskite thickness (~600 nm) with an average rms-roughness of 30 nm after subtracting the TiO_2 corrugation [Fig. 3(a) orange curve]. Importantly, the height variations cancel out almost completely, which further strengthens the assumption that the perovskite thickness is very homogeneous.

We concluded that the variations in Q_e^{lum}, as observed in Fig. 2, arose from the mesoporous-TiO_2, with an average period of ~80 μm and height of ~100 nm for the hills and valleys. This was further reinforced by the PL measurement performed at the same spot as shown

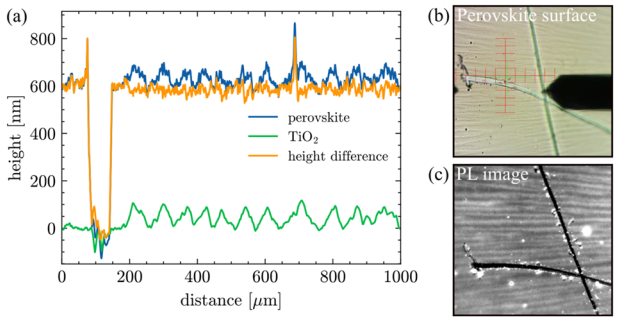

FIG. 3. (a) Line profiles across the scratch on, the perovskite surface (blue) and mp-TiO_2 surface (green). The orange curve is the remaining corrugation of the perovskite after subtraction of the mp-TiO_2 height variations. (b) Region of the perovskite surface scanned with the profilometer tip and scan direction (vertically up). (c) PL intensity map of the same region as (b).

in Fig. 3(c), where a bright and dark contrast is observed, originating from the same hills and valleys, respectively. Therefore, we concluded that thickness variations of the perovskite, which could change τ_{surf}, are not responsible for the observed changes in Q_e^{lum}.

In the next step, the origin of the Q_e^{lum} variations arising from the inhomogeneous mesoporous TiO_2 will be further analyzed. We carried out TRPL measurements on the two sets of absorbers (passivated and unpassivated) in two different geometries, as shown in the insets of Figs. 4(a) and 4(b). In all measurements, the laser flux and repetition frequency were kept constant. In Fig. 4(a), the perovskite side was illuminated, which means that most of the photons were absorbed far away from the mesoporous-TiO_2 interface. This situation is similar to the one used in Fig. 2. In the next step, the sample was flipped 180°, and the measurements were repeated. The results are shown in Fig. 4(b), and in this case, most of the photons were absorbed close to the mesoporous-TiO_2 interface.

Krogmeier et al.[18] showed that the transfer of carriers to the extraction layer will cause a reduction in the PL signal at an early time (extending some tens of nanoseconds after the pulse), which is not caused by recombination. Our measurements performed in the two different geometries can be used to quantify this extraction since the *np* product at the interface is strongly changed, which should also impact the TRPL transients. In the absence of a high surface/interface recombination velocity, the initial drop can, therefore, be assigned unambiguously to a charge-transfer process. However, a similar fast initial drop should occur in the case of a high surface recombination velocity; therefore, the comparison between passivated and non-passivated surfaces is crucial to distinguish between the two cases.

The first observation is that the TRPL transients measured from the perovskite side are different for passivated and unpassivated absorbers [see Fig. 4(a)]. For the passivated case, we observed an almost completely mono-exponential decay with an effective lifetime of ~500 ns. The long decay time for the unpassivated absorbers is reduced by approximately a factor of two, i.e., only 250 ns. This difference is also visible in the differential lifetime plots shown in the supplementary material (Fig. S4).

Furthermore, the initial slopes right after the laser pulse were different. We observed a fast initial decay for the unpassivated

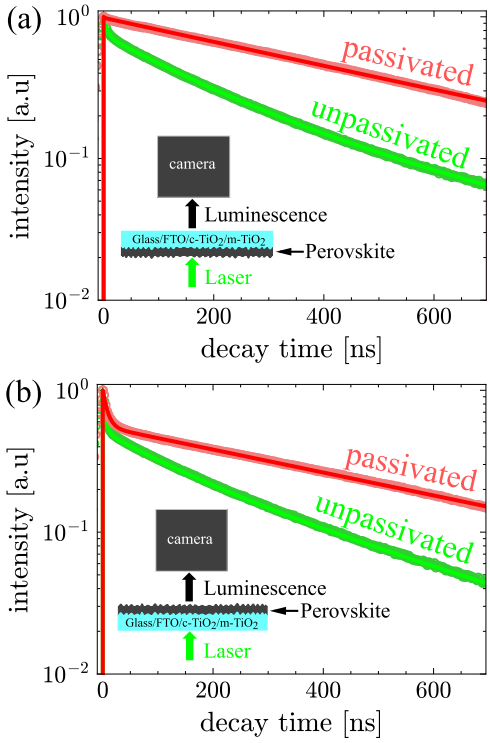

FIG. 4. Transient photoluminescence measurements acquired on a perovskite film with illumination from (a) the perovskite side and (b) the glass side. The insets show a schematic representation of the measurement configuration. Green and red represent unpassivated and passivated samples, respectively, which are fitted using mono- or bi-exponential decay functions. The laser injection in all cases was 1.2 nJ/cm^2.

absorber that was absent for the passivated case. Measurements made on the glass side, which is close to the TiO_2 interface, showed fast initial drops for both absorbers, independent of the passivation layer [see Fig. 4(b)]. In the following, we develop a model for the observed changes.

In the first step, we need to understand whether the measurements were performed under low- or high-injection conditions since this also impacts the shape of the TRPL transients. We note that from the extracted lifetime of the passivated absorber (500 ns) and the measured Q_e^{lum}-value $(3.5 \cdot 10^{-3})$, we can estimate the bulk doping of the perovskite via Eq. (3). For an absorption coefficient of $\sim 1 \cdot 10^5$ cm^{-1}, we deduce a value of $1 \cdot 10^{15}$ cm^{-3}, assuming a radiative recombination coefficient $k_{rad} = 6 \cdot 10^{-11}$ cm^3/s and $p_e = 0.1$.[14] The measurements were conducted with a photon density per pulse of $2.4 \cdot 10^{14}$ cm^{-3}. Consequently, the measurements were performed under low injection conditions as $\Delta n < N_A$. This also explains why we do see a mono-exponential decay for the passivated absorber measured from the perovskite side, as shown in Fig. 4(a).

In the next step, we can estimate the surface recombination velocity S. From the differential lifetime, defined as $1/\tau_{diff} = -\frac{d}{dt} \ln(I_{PL}(t))$, we can estimate S for the two cases from the initial steep decay right after the pulse[15] [Eq. (175)] via

$$S = \frac{1}{\alpha}\left(\frac{1}{\tau_{\mathrm{diff}}(t=0)} - \frac{1}{\tau}\right). \quad (6)$$

The absorption coefficient is defined as α, and τ refers to the minority carrier lifetime for long decay times. We use the deduced τ-values from the TRPL measurements shown in Figs. 4(a) and 4(b) to estimate S, assuming $\alpha = 1 \cdot 10^5\ \mathrm{cm}^{-1}$. The $\tau_{\mathrm{diff}}(t=0)$ for unpassivated (27 ns) and for passivated (200 ns) is taken from the differential lifetime plot of Fig. 4, shown in supplementary material (Fig. S4). The deduced values are ~240 cm/s for the unpassivated absorbers, whereas for the passivated case, the values drop to only 30 cm/s. Plugging these values into Eq. (5) yields surface lifetimes of 1 μs for the passivated case and 125 ns for the unpassivated absorber. Equation (5) assumes that both interfaces exhibit the same interface recombination velocity, which may not be true since the perovskite surface is in contact with N_2 and the back side is in contact with TiO_2. If we assume the extreme case of no interface recombination on the back surface, Eq. (3) is slightly modified,[14] and we end up with a value of 250 ns instead of 125 ns. Comparing these values with the values derived from our TRPL measurements in Fig. 4, we see that the passivated case τ_{eff} is not limited by surface recombination, while the unpassivated case τ_{eff} is limited by the interface recombination velocity S. For the case of identical interface recombination velocities at both surfaces, the values are lower than the long decay times, whereas for a perfectly passivated rear surface, we find very good agreement. This is a hint that the TiO_2 interface is well passivated. For the case where the perovskite side is illuminated, we conclude that the initial fast drop in the unpassivated case is due to a high surface recombination velocity, which impacts the region right after the pulse but also reduces the decay times at later times. The passivated case does not show signs of dominant interface recombination, and the extracted lifetimes reflect the true bulk minority carrier lifetime in agreement with the observed mono-exponential decay.

The TRPL measurements performed on the other geometry, that is, from the glass side, as presented in Fig. 4(b), are distinct from those in which the illumination was performed from the perovskite side. The differential lifetimes are very short right after the pulse and, after ~50 ns, converge toward the same values as for the perovskite side illumination. Shortly after the pulse, we find $\tau_{\mathrm{diff}} = 12$ ns for the unpassivated case and $\tau_{\mathrm{diff}} = 17$ ns for the passivated case. If we use the same reasoning as before, we directly see that the τ_{diff} values right after the pulse for the passivated case are not compatible with the long τ_{eff} values of 500 ns if we relate them to interface recombination. Therefore, the fast drop measured immediately after the pulse can be assigned with high certainty to charge extraction at the TiO_2 interface, in agreement with the simulations performed by Krogmeier *et al.*[18] This is also the reason why we do see the same effect on both passivated and non-passivated absorbers. The surface recombination velocity at the perovskite surface is not relevant. The surface recombination velocity at the TiO_2 interface is low, as otherwise, we would not be able to measure a lifetime of 500 ns for the passivated case. Consequently, the only possibility remaining is that TiO_2 induces a fast initial decay due to carrier extraction.

Having established a model that explains the observed average transients, we will now discuss the laterally resolved TRPL measurements in more detail. Due to the low injection conditions, the signal at a single-pixel level is very weak, making it difficult to extract transients with a good signal-to-noise ratio. Consequently, we divided the image into two components, one denoted as hills and the other as valleys. To separate the two components, we used a two-dimensional Fast Fourier transform (FFT) to identify the hills and valley regions using the program Gwyddion.[35] The Fourier transformation allowed us to identify the characteristic frequencies in the images, which were, in our case, the variations in the PL counts imposed by the changes in TiO_2 thickness. In the second step, only these frequencies were masked and extracted from the image. The generated image has the same modulated pattern, albeit with a much better signal-to-noise ratio. We then used this image to generate a binary image that we used as a mask to filter out the hills and valleys in the original images. The procedure is shown in supplementary material (Fig. S5).

For this analysis, we used glass side illumination, where the interface is common for both passivated and unpassivated samples. The results of the identification of the hills and valleys and the transients extracted are shown in Fig. 5. In the present case, the valleys were highlighted with a green overlay. Figure 5(b) shows the TRPL transients extracted from both regions, which were then used to compute the differential lifetimes depicted in the bottom plot of Fig. 5(b). The hills and valleys showed $\tau_{\mathrm{diff}} = 30$ ns and $\tau_{\mathrm{diff}} = 17$ ns, respectively, right after the pulse. After ~100 ns, both curves converged to the same value of ~200 ns, in agreement with the averaged data presented in Fig. 4.

Low initial differential lifetimes are indicative of a fast process taking place right after the pulse. The valleys exhibited smaller values, which meant that in such regions, the extraction is faster. The faster carrier extraction leads to an overall reduction in the TRPL signal, as shown in Fig. 5(b). This reduction could also explain the measurements shown in Fig. 2, where the integrated PL signal at high repetition frequency was used to generate Q_e^{lum}-maps. However, under open-circuit conditions, which is the case for steady-state PL, there will be no net flow of carriers, and consequently, a constant drain of electrons from the perovskite to the TiO_2 will not take place. An additional recombination channel that reduces Q_e^{lum} must be active. It is known from the literature that the thickness of the TiO_2 extraction layer needs to be fine-tuned to achieve maximum performance. Furthermore, the TiO_2 layer needs to be doped to increase conductivity and improve band alignment with the perovskite film. The low thickness of mp-TiO_2 in the valleys is sufficient to allow efficient extraction of charge carriers, as illustrated by the small effective lifetimes; however, the recombination activity needs to be enhanced, which consequently leads to Q_e^{lum} losses and, therefore, V_{OC} losses in the final device.

Consequently, we attribute the differences between the hills and valleys to a slight modification of the conduction and valence bands coupled with a change in the recombination rate at this interface. It has been shown that the conduction band can be effectively changed via Li-doping. In the present case, we used Li-TFSI to enhance charge carrier extraction and reduce the trap density within the TiO_2 layer. However, the mp-TiO_2 thickness is not constant at all, with height variations up to 100 nm, as shown in Fig. 3. Therefore, the ratio between mp-TiO_2 and Li-TFSI has changed substantially, and this will certainly affect the electrical properties of mp-TiO_2. As a consequence, the TiO_2 properties vary on the length scale of ~80 μm, with adverse effects on device performance. It will be imperative to improve the thickness homogeneity of the mp-TiO_2 layer to further improve the device's performance.

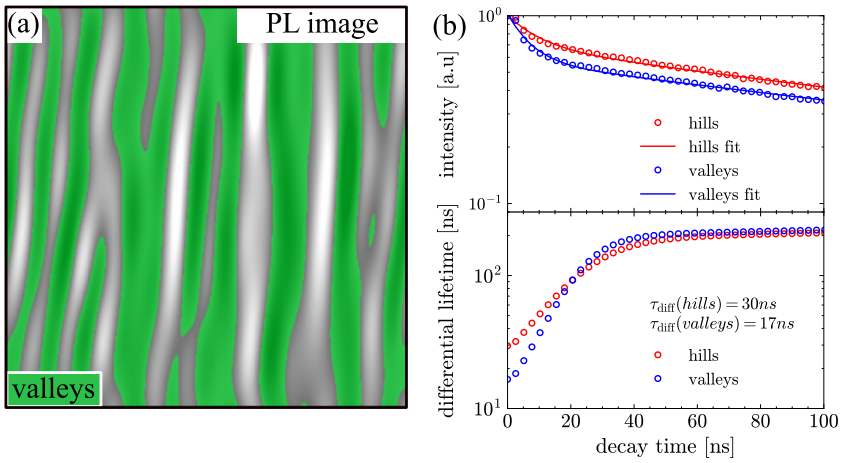

FIG. 5. Transient photoluminescence extracted from strip pattern: (a) PL image taken from the glass side (backside) of perovskite. The image has been treated with 2D-Fast Fourier transform (FFT) to have noise-free visibility of the hills and valleys. A green mask is used to separate the valleys and hills. (b) PL transient and differential lifetime extracted from hills and valleys seen from (a).

V. CONCLUSION

Improving the power conversion efficiency of halide perovskites well beyond 20% requires fine-tuning all the properties of each layer. Here, we used photoluminescence imaging to deconvolute the various recombination and charge extraction processes occurring at the top surface and bottom interface of the state-of-the-art $(FAPbI_3)_{0.97}(MAPbBr_3)_{0.03}$ perovskite absorbers. We find that passivation with a thin layer of the organic molecule biphenyl-4 4′-dithiol reduces the surface recombination velocity at the perovskite/N_2 interface by approximately one order of magnitude (from 240 cm/s for the unpassivated one to 29 cm/s for the passivated one), causing an order of magnitude boost in Q_e^{lum}. The rear surface of the perovskite, which is in contact with a mesoporous TiO_2 layer, exhibits fast initial decay times, consistent with rapid electron charge extraction. However, periodic thickness variations of the mp-TiO_2 on the order of 100 nm lead to varying charge carrier extraction velocities, which also impact the photoluminescence quantum yields and consequently V_{OC}. To further improve device efficiency, a more homogeneous TiO_2 layer needs to be developed.

SUPPLEMENTARY MATERIAL

All the additional information and details in support of this paper are provided in the supplementary material.

ACKNOWLEDGMENTS

This research was funded in whole, or in part, by the Luxembourg National Research Fund (FNR), Grant Reference [Nos. 11244141, 14757355, and 12246511]. The authors acknowledge technical support by B. Uder, U. Siegel, and R. Himelrick.

AUTHOR DECLARATIONS

Conflict of Interest

The authors have no conflicts to disclose.

Author Contributions

H. Phirke: Conceptualization (equal); Formal analysis (lead); Investigation (lead); Methodology (lead); Visualization (equal); Writing – original draft (lead). **S. Gharabeiki**: Resources (equal). **A. Singh**: Investigation (equal); Methodology (supporting). **A. Krishna**: Resources (equal). **S. Siebentritt**: Resources (supporting); Supervision (lead). **A. Redinger**: Conceptualization (equal); Methodology (lead); Resources (supporting); Supervision (lead); Writing – review & editing (equal).

DATA AVAILABILITY

The data that support the findings of this study are available within the article and its supplementary material.

REFERENCES

[1] M. A. Green, E. D. Dunlop, M. Yoshita, N. Kopidakis, K. Bothe, G. Siefer, and X. Hao, "Solar cell efficiency tables (version 62)," Prog. Photovoltaics **31**, 651–663 (2023).

[2] J. Burschka, N. Pellet, S. J. Moon, R. Humphry-Baker, P. Gao, M. K. Nazeeruddin, and M. Grätzel, "Sequential deposition as a route to high-performance perovskite-sensitized solar cells," Nature **499**, 316–319 (2013).

[3] J. H. Noh, S. H. Im, J. H. Heo, T. N. Mandal, and S. I. Seok, "Chemical management for colorful, efficient, and stable inorganic–organic hybrid nanostructured solar cells," Nano Lett. **13**, 1764–1769 (2013).

[4] G. E. Eperon, S. D. Stranks, C. Menelaou, M. B. Johnston, L. M. Herz, and H. J. Snaith, "Formamidinium lead trihalide: A broadly tunable perovskite for efficient planar heterojunction solar cells," Energy Environ. Sci. **7**, 982–988 (2014).

[5] G. Xing, N. Mathews, S. S. Lim, N. Yantara, X. Liu, D. Sabba, M. Grätzel, S. Mhaisalkar, and T. C. Sum, "Low-temperature solution-processed wavelength-tunable perovskites for lasing," Nat. Mater. **13**, 476–480 (2014).

[6] Z. K. Tan, R. S. Moghaddam, M. L. Lai, P. Docampo, R. Higler, F. Deschler, M. Price, A. Sadhanala, L. M. Pazos, D. Credgington, F. Hanusch, T. Bein, H. J. Snaith, and R. H. Friend, "Bright light-emitting diodes based on organometal halide perovskite," Nat. Nanotechnol. **9**, 687–692 (2014).

[7]F. Deschler, M. Price, S. Pathak, L. E. Klintberg, D. D. Jarausch, R. Higler, S. Hüttner, T. Leijtens, S. D. Stranks, H. J. Snaith, M. Atatüre, R. T. Phillips, and R. H. Friend, "High photoluminescence efficiency and optically pumped lasing in solution-processed mixed halide perovskite semiconductors," J. Phys. Chem. Lett. **5**, 1421–1426 (2014).
[8]S. D. Stranks and H. J. Snaith, "Metal-halide perovskites for photovoltaic and light-emitting devices," Nat. Nanotechnol. **10**, 391–402 (2015).
[9]Q. Dong *et al.*, "Electron-hole diffusion lengths >175 μm in solution-grown $CH_3NH_3PbI_3$ single crystals," Science **347**, 967–970 (2015).
[10]M. Baranowski and P. Plochocka, "Excitons in metal-halide perovskites," Adv. Energy Mater. **10**, 1903659 (2020).
[11]Y. Bi, E. M. Hutter, Y. Fang, Q. Dong, J. Huang, and T. J. Savenije, "Charge carrier lifetimes exceeding 15 μs in methylammonium lead iodide single crystals," J. Phys. Chem. Lett. **7**, 923–928 (2016).
[12]Z. Liu, L. Krückemeier, B. Krogmeier, B. Klingebiel, J. A. Márquez, S. Levcenko, S. Öz, S. Mathur, U. Rau, T. Unold, and T. Kirchartz, "Open-circuit voltages exceeding 1.26 V in planar methylammonium lead iodide perovskite solar cells," ACS Energy Lett. **4**, 110–117 (2019).
[13]T. Kirchartz, J. A. Márquez, M. Stolterfoht, and T. Unold, "Photoluminescence-based characterization of halide perovskites for photovoltaics," Adv. Energy Mater. **10**, 1904134 (2020).
[14]F. Staub, H. Hempel, J.-C. Hebig, J. Mock, U. W. Paetzold, U. Rau, T. Unold, and T. Kirchartz, "Beyond bulk lifetimes: Insights into lead halide perovskite films from time-resolved photoluminescence," Phys. Rev. Appl. **6**, 044017 (2016).
[15]R. K. Ahrenkiel, "Chapter 2 minority-carrier lifetime in III–V semiconductors," Semicond. Semimetals **39**, 39–150 (1993).
[16]M. Stolterfoht, P. Caprioglio, C. M. Wolff, J. A. Márquez, J. Nordmann, S. Zhang, D. Rothhardt, U. Hörmann, Y. Amir, A. Redinger, L. Kegelmann, F. Zu, S. Albrecht, N. Koch, T. Kirchartz, M. Saliba, T. Unold, and D. Neher, "The impact of energy alignment and interfacial recombination on the internal and external open-circuit voltage of perovskite solar cells," Energy Environ. Sci. **12**, 2778–2788 (2019).
[17]J. Haddad, B. Krogmeier, B. Klingebiel, L. Krückemeier, S. Melhem, Z. Liu, J. Hüpkes, S. Mathur, and T. Kirchartz, "Analyzing interface recombination in lead-halide perovskite solar cells with organic and inorganic hole-transport layers," Adv. Mater. Interfaces **7**, 2000366 (2020).
[18]B. Krogmeier, F. Staub, D. Grabowski, U. Rau, and T. Kirchartz, "Quantitative analysis of the transient photoluminescence of $CH_3NH_3PbI_3/PC_{61}BM$ heterojunctions by numerical simulations," Sustainable Energy Fuels **2**, 1027–1034 (2018).
[19]E. M. Hutter, T. Kirchartz, B. Ehrler, D. Cahen, and E. von Hauff, "Pitfalls and prospects of optical spectroscopy to characterize perovskite-transport layer interfaces," Appl. Phys. Lett. **116**, 100501 (2020).
[20]J. Hidalgo, A. F. Castro-Méndez, and J. P. Correa-Baena, "Imaging and mapping characterization tools for perovskite solar cells," Adv. Energy Mater. **9**, 1900444 (2019).
[21]M. C. Schubert, L. E. Mundt, D. Walter, A. Fell, and S. W. Glunz, "Spatially resolved performance analysis for perovskite solar cells," Adv. Energy Mater. **10**, 1904001 (2020).
[22]Z. Ni, S. Xu, H. Jiao, H. Gu, C. Fei, and J. Huang, "High grain boundary recombination velocity in polycrystalline metal halide perovskites," Sci. Adv. **8**, eabq8345 (2022).
[23]A. Delamarre, L. Lombez, and J. F. Guillemoles, "Contactless mapping of saturation currents of solar cells by photoluminescence," Appl. Phys. Lett. **100**, 8–11 (2012).
[24]M. Stolterfoht, C. M. Wolff, J. A. Márquez, S. Zhang, C. J. Hages, D. Rothhardt, S. Albrecht, P. L. Burn, P. Meredith, T. Unold, and D. Neher, "Visualization and suppression of interfacial recombination for high-efficiency large-area pin perovskite solar cells," Nat. Energy **3**, 847–854 (2018).
[25]T. Trupke, B. Mitchell, J. W. Weber, W. McMillan, R. A. Bardos, and R. Kroeze, "Photoluminescence imaging for photovoltaic applications," Energy Procedia **15**, 135–146 (2012).
[26]G. Rey, O. Kunz, M. Green, and T. Trupke, "Luminescence imaging of solar modules in full sunlight using ultranarrow bandpass filters," Prog. Photovoltaics **30**, 1115–1121 (2022).
[27]G. El-Hajje, C. Momblona, L. Gil-Escrig, J. Ávila, T. Guillemot, J. F. Guillemoles, M. Sessolo, H. J. Bolink, and L. Lombez, "Quantification of spatial inhomogeneity in perovskite solar cells by hyperspectral luminescence imaging," Energy Environ. Sci. **9**, 2286–2294 (2016).
[28]D. W. DeQuilettes, S. M. Vorpahl, S. D. Stranks, H. Nagaoka, G. E. Eperon, M. E. Ziffer, H. J. Snaith, and D. S. Ginger, "Impact of microstructure on local carrier lifetime in perovskite solar cells," Science **348**, 683–686 (2015).
[29]Z. Hameiri, A. Mahboubi Soufiani, M. K. Juhl, L. Jiang, F. Huang, Y. B. Cheng, H. Kampwerth, J. W. Weber, M. A. Green, and T. Trupke, "Photoluminescence and electroluminescence imaging of perovskite solar cells," Prog. Photovoltaics **23**, 1697–1705 (2015).
[30]S. Cacovich, G. Vidon, M. Degani, M. Legrand, L. Gouda, J. B. Puel, Y. Vaynzof, J. F. Guillemoles, D. Ory, and G. Grancini, "Imaging and quantifying non-radiative losses at 23% efficient inverted perovskite solar cells interfaces," Nat. Commun. **13**, 2868 (2022).
[31]L. Wagner, P. Schygulla, J. P. Herterich, M. Elshamy, D. Bogachuk, S. Zouhair, S. Mastroianni, U. Würfel, Y. Liu, S. M. Zakeeruddin, M. Grätzel, A. Hinsch, and S. W. Glunz, "Revealing fundamentals of charge extraction in photovoltaic devices through potentiostatic photoluminescence imaging," Matter **5**, 2352–2364 (2022).
[32]D. Yamashita, T. Handa, T. Ihara, H. Tahara, A. Shimazaki, A. Wakamiya, and Y. Kanemitsu, "Charge injection at the heterointerface in perovskite $CH_3NH_3PbI_3$ solar cells studied by simultaneous microscopic photoluminescence and photocurrent imaging spectroscopy," J. Phys. Chem. Lett. **7**, 3186–3191 (2016).
[33]A. Krishna, H. Zhang, Z. Zhou, T. Gallet, M. Dankl, O. Ouellette, F. T. Eickemeyer, F. Fu, S. Sanchez, M. Mensi, S. M. Zakeeruddin, U. Rothlisberger, G. N. Manjunatha Reddy, A. Redinger, M. Grätzel, and A. Hagfeldt, "Nanoscale interfacial engineering enables highly stable and efficient perovskite photovoltaics," Energy Environ. Sci. **14**, 5552–5562 (2021).
[34]A. Krishna, V. Škorjanc, M. Dankl, J. Hieulle, H. Phirke, A. Singh, E. A. Alharbi, H. Zhang, F. Eickemeyer, S. M. Zakeeruddin, G. N. M. Reddy, A. Redinger, U. Rothlisberger, M. Grätzel, and A. Hagfeldt, "Mitigating the heterointerface driven instability in perovskite photovoltaics," ACS Energy Lett. **8**, 3604–3613 (2023).
[35]D. Nečas and P. Klapetek, "Gwyddion: An open-source software for SPM data analysis," Open Phys. **10**, 181–188 (2012).